One-step electrosynthesis of MnO_2/rGO nanocomposite and its enhanced electrochemical performance

Gomaa A.M. Ali[a,b], Mashitah M. Yusoff[a], H. Algarni[c,d], Kwok Feng Chong[a,*]

[a] Faculty of Industrial Sciences & Technology, Universiti Malaysia Pahang, Kuantan, 26300 Gambang, Pahang, Malaysia
[b] Chemistry Department, Faculty of Science, Al–Azhar University, Assiut 71524, Egypt
[c] Research Centre for Advanced Materials Science (RCAMS), King Khalid University, P. O. Box 9004, Abha 61413, Saudi Arabia
[d] Department of Physics, Faculty of Sciences, King Khalid University, P. O. Box 9004, Abha, Saudi Arabia

ARTICLE INFO

ABSTRACT

We present a facile one-step electrochemical approach to generate MnO_2/rGO nanocomposite from a mixture of Mn_3O_4 and graphene oxide (GO). The electrochemical conversion of Mn_3O_4 into MnO_2 through potential cycling is expedited in the presence of GO while the GO is reduced into reduced graphene oxide (rGO). The MnO_2 nanoparticles are evenly distributed on the rGO nanosheets and act as the spacer to prevent rGO nanosheets from restacking. This unique structure provides high electroactive surface area ($1173\,m^2\,g^{-1}$) that improves ions diffusion within the MnO_2/rGO structure. As a result, the MnO_2/rGO nanocomposite exhibits high specific capacitance of $473\,F\,g^{-1}$ at $0.25\,A\,g^{-1}$, which is remarkably higher (3 times) than the Mn_3O_4/GO prior conversion. In addition, the electrosynthesized nanocomposite shows higher conductivity and excellent potential cycling stability of 95% at 2000 cycles.

1. Introduction

A modern technological society requires an efficient energy storage system which can supply huge amount of energy within a short period of time. Conventional energy storage systems such as capacitors and batteries are limited by the low energy density and slow power output, respectively. In this context, supercapacitors can bridge the gap between capacitors and batteries, to provide higher energy density ($5\,Wh\,kg^{-1}$) and greater power output ($10\,kW\,kg^{-1}$) in addition to higher cycling stability [1]. Supercapacitors store energy in two different modes, either in double layer capacitance mode through ions adsorption, or in pseudocapacitance mode through faradaic reaction [2–8]. In most cases, supercapacitors in pseudocapacitance mode provide higher energy density than those in double layer capacitance mode as higher amount charge is transferred in the faradaic process in pseudocapacitance mode. Ironically, this charge transfer process causes physical and chemical changes during prolonged charge-discharge process, therefore reducing their durability as compared to the supercapacitors in double layer capacitance mode. Among the pseudocapacitive materials, manganese oxides (Mn_xO_y) show promising potential as the supercapacitors electrode owing to their natural abundance, low cost, low toxicity and high theoretical specific capacitance ($1370\,F\,g^{-1}$) [1,9–13]. Mn_3O_4 was reported to possess charge storage up to $70\,F\,g^{-1}$

in Na_2SO_4 electrolyte [14]. However, the application of Mn_3O_4 as a practical electrode is limited by the intrinsic low conductivity of the material (10^{-6}–10^{-9} $S\,cm^{-1}$) [15,16]. Another class of manganese oxide in +4 oxidation state, MnO_2 was proven to have comparatively higher conductivity (10^{-3}–10^{-6} S cm^{-1}) and exhibit good charge storage up to $210\,F\,g^{-1}$ at $0.2\,A\,g^{-1}$ in Na_2SO_4 electrolyte [10,17,18]. Studies showed that its rate performance and electrical conductivity could be improved by incorporating high conductivity nanomaterial, such as MnO_2/CNTs–CNFs [19], MnO_2/rGO [20], $CoMnO_2$/VGCF [21], etc.

On the other hand, graphene or reduced graphene oxide (rGO) is gaining interest as the supercapacitors electrode, owing to its high electrical conductivity (5×10^{-3} $S\,cm^{-1}$), rich electrochemistry and high specific surface area ($2630\,m^2\,g^{-1}$) [22–25]. If the entire surface area of graphene is fully utilized, a specific capacitance of $550\,F\,g^{-1}$ could be achieved [26]. Nonetheless, the reported specific capacitance values for graphene or rGO materials are merely in the range of 80–$264\,F\,g^{-1}$ in aqueous electrolytes [22,26–28], which can be attributed by the restacking or agglomeration of rGO nanosheets that causes the reduce in electrochemically active surface area. The advancement in nanotechnology renders the engineering of graphene materials to incorporate pseudocapacitive materials such as Co_3O_4, Fe_3O_4, SnO_2, ZnO and MnO_2 in forming the new composite materials

G.A.M. Ali et al.
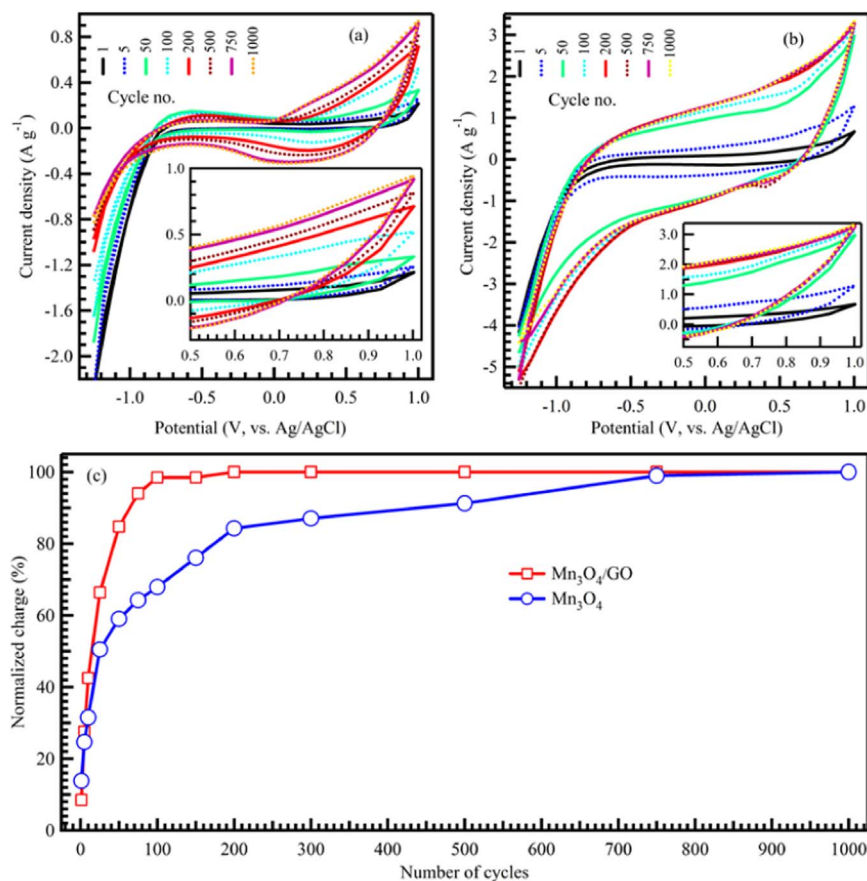
Fig. 1. Cyclic voltammetry curves for (a) Mn_3O_4, (b) Mn_3O_4/GO and (c) normalized charge as a function of cycle number for Mn_3O_4 and Mn_3O_4/GO during the potential cycling.
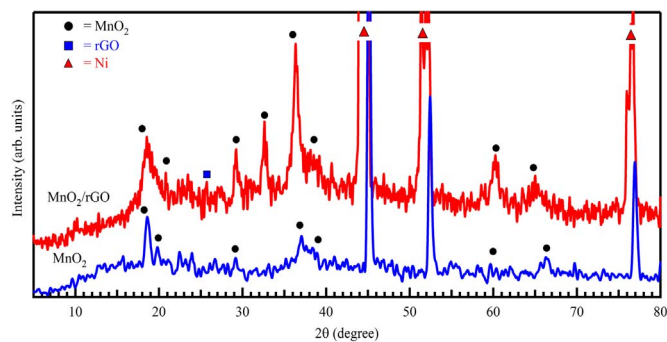
Fig. 2. XRD patterns of MnO_2 and MnO_2/rGO.

for supercapacitors electrode [29–33]. Both components in the composite act as the spacers to each other to minimize the restacking and agglomeration, therefore increase the effective surface area accessible to the electrolyte. Furthermore, graphene materials offer a conductive platform for fast electron mobility but their double layer capacitive charge storage are often limited. Conversely, pseudocapacitive materials possess high specific capacitance, but low in conductivity [34,35]. Therefore, they complement each other in the composite materials. The non-faradaic energy storage mechanism in graphene also offers high potential cycling stability to the pseudocapacitive materials, which tend to degrade after prolonged potential cycling. The benefits of these composite materials have accelerated the advancement of MnO_2/graphene nanocomposites, which can be fabricated by different techniques, such as electrostatic assembly, chemical vapor deposition followed by hydrothermal microwave irradiation, two successive electrochemical deposition process, liquid phase exfoliation and hydrothermal methods, etc [36–38]. In spite of the considerable progress in the fabrication of MnO_2/graphene nanocomposites, it remains a

major challenge to design a simple yet efficient method to produce this composite material with outstanding electrochemical performance. In this work, a facile electrochemical approach is introduced to produce MnO_2/rGO at higher conversion rate and its enhanced electrochemical performance as supercapacitors electrode is also discussed.

2. Experimental procedures

2.1. Samples preparation

Graphene oxide (GO) was prepared by Hummers' method as described in detail elsewhere [24]. Briefly, graphite powder (Merck) was pre-oxidized by slowly mixing 20 g of graphite, 10 g of $K_2S_2O_8$ and 10 g of P_2O_5 into 30 mL of concentrated H_2SO_4. The reaction mixture was heated up to 80 °C using an oil bath with continuous stirring for 6 h. The mixture was then filtered, washed and dried. To oxidize the powder, 20 g of the pre-oxidized graphite powder was added to 460 mL of concentrated H_2SO_4 in an ice bath. 60 g of $KMnO_4$ was then slowly added into the mixture. The temperature was maintained at 35 °C for 2 h with stirring before 3 L of distilled water and 50 mL of 30% H_2O_2 were added to the mixture. The mixture was filtered, washed with 1:10 aqueous HCl solution and dried overnight at 60 °C in vacuum. Exfoliation of graphite oxide was done by sonicating graphite oxide dispersion ($2\,g\,L^{-1}$) at 200 W for 30 min. The dispersion was later centrifuged at 6000 rpm for 10 min to remove the unexfoliated graphite oxide. The GO powder was obtained by filtering the homogeneous yellow-brown supernatant and dried under vacuum overnight.

Mn_3O_4 was prepared as reported elsewhere [39]. Firstly, equal amount of Na_2CO_3 aqueous solution ($0.07\,g\,mL^{-1}$) and $MnSO_4{\cdot}H_2O$ ethanolic solution ($0.022\,g\,mL^{-1}$) were mixed and then stirred for 3 h at room temperature. The obtained brown precipitates of Mn_3O_4 was filtered and washed with distilled water and ethanol before final drying

G.A.M. Ali et al.
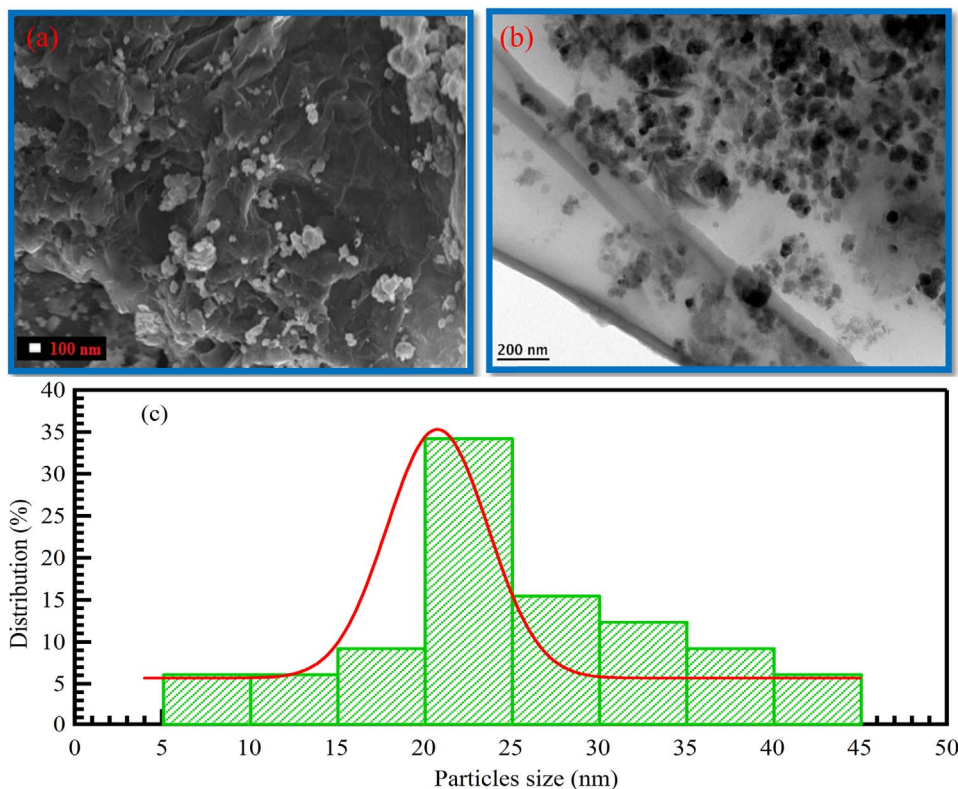
Fig. 3. (a) FESEM, (b) TEM images and (c) particles size distribution for MnO$_2$/rGO.
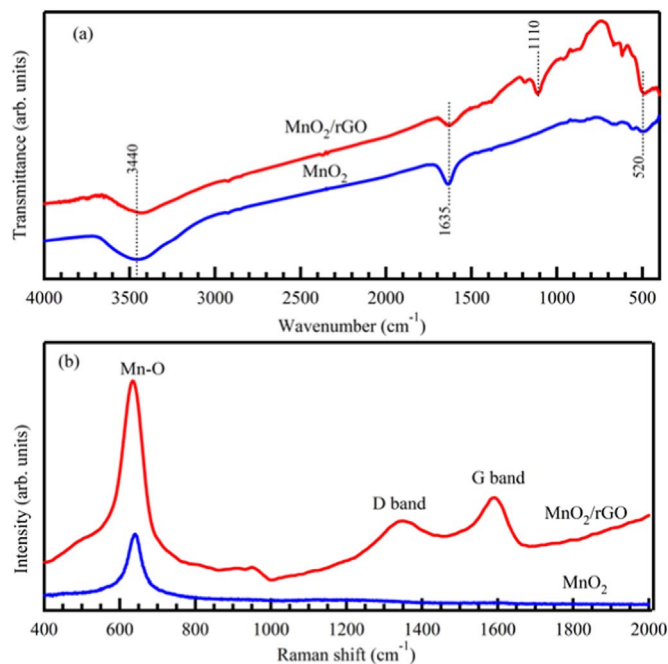
Fig. 4. (a) FTIR and (b) Raman spectra of MnO$_2$ and MnO$_2$/rGO.

at 60 °C for 12 h.

The Mn$_3$O$_4$/GO electrode was prepared by mixing the active material (GO powder and Mn$_3$O$_4$ powder in 1:1 wt ratio) and subsequently coated onto a nickel foam (ca. 4 mg). All the results obtained in electrochemical study were normalized by the active material mass to obtain gravimetric capacitance (F/g). Three-electrode system was setup in 1 M Na$_2$SO$_4$ with Mn$_3$O$_4$/GO electrode as a working electrode, Pt wire as a counter electrode and Ag/AgCl as a reference electrode. The electrochemical conversion was performed by running cyclic voltammetry at the potential window between −1.2 V and 1.0 V at 50 mV s^{-1}. A similar setup was deployed for Mn$_3$O$_4$ electrode as control experiment.

2.2. Sample characterizations

The crystal structure was analyzed using a Rigaku X-ray diffractometer (Miniflex II with Cu-K$_\alpha$ radiation at 40 kV, 30 mA, λ = 1.5406 Å) within the 2θ range of 5–80° at a scanning rate of 0.02 θ s^{-1} with a step time of 2 s. The surface morphology was monitored by a JEOL (JEM2100F) transmission electron microscope (TEM) and a JEOL (JSM7800F) field emission scanning electron microscope (FESEM). The functional groups were examined using a Perkin Elmer (Spectrum 100) infrared spectrophotometer over the range of 400–4000 cm^{-1}. Raman spectra were obtained using a Renishaw Raman microscope (InVia) with 532 nm laser excitation.

2.3. Electrochemical measurements

The electrochemical properties were measured in 1 M Na$_2$SO$_4$ electrolyte using a three-electrode system with the active material as a working electrode, Ag/AgCl as a reference electrode and Pt wire as a counter electrode. The data were collected using an Autolab (PGSTAT M101) electrochemical workstation equipped with frequency response analyzer. The potential was scanned between 0 and 1 V with different scan rates between 2 and 100 mV s^{-1}. Charge-discharge galvanostatic tests were performed at current density ranged from 0.2 to 1 A g^{-1}. Impedance data were collected from 100 kHz to 0.01 Hz, at open circuit potential with an AC signal of 10 mV in amplitude in 1 M Na$_2$SO$_4$ in the dark. Mott-Schottky data were collected by testing the impedance at different applied potentials (−1 to 1 V) to determine the flat band potential.
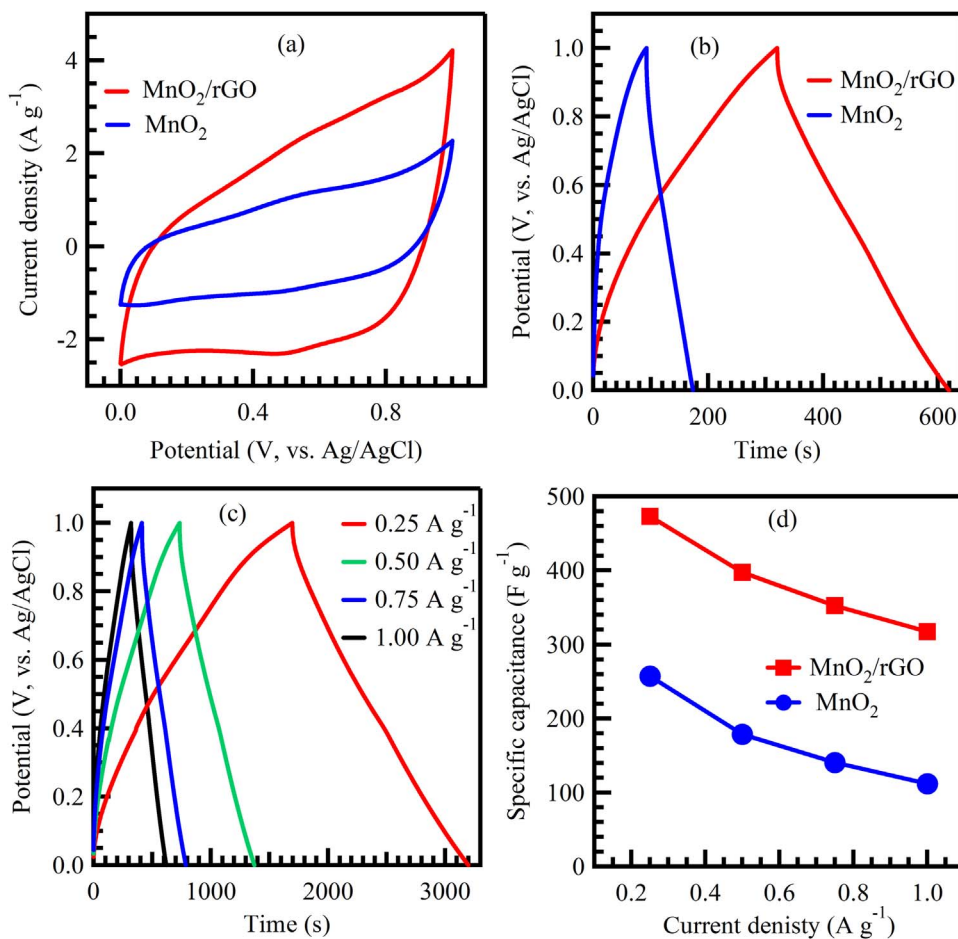
Fig. 5. (a) Cyclic voltammetry curves at $10\,mV\,s^{-1}$ (b) galvanostatic charge-discharge curves at $1\,A\,g^{-1}$, (c) galvanostatic charge-discharge curves different current densities for MnO_2/rGO and (d) specific capacitance as a function of current density for MnO_2 and MnO_2/rGO.

3. Results and discussion

Our previous work demonstrated the successful conversion of Mn_3O_4 into MnO_2 upon potential cycling [12]. Fig. 1a shows the CV conversion to form MnO_2 with the area under the curve (also referred to charge) increases with increasing cycle number. As explained in our previous work, oxidation of Mn atom occurred at the anodic scan while intercalation of sodium ions occurred at the cathodic scan; the continuous potential cycling between anodic and cathodic scans converted all Mn_3O_4 into MnO_2. The complete conversion occurs at ca. 750th cycle where there is no increment in the charge density. Upon addition of GO into Mn_3O_4 followed by potential cycling, Mn_3O_4 was oxidized into MnO_2 and GO was reduced to rGO simultaneously. The CV conversion to form MnO_2/rGO is shown in Fig. 1b. Similar to MnO_2 formation, the charge for MnO_2/rGO formation increases with increasing cycle number. However, it is worth mentioning that the charge ceases to increase after ca. 200th cycle, indicating the complete conversion into MnO_2/rGO. The charge increment with respects to cycle number is summarized in Fig. 1c. For MnO_2/rGO, the charge increases drastically for each potential cycle and complete conversion occurs at ca. 200th cycle, as compared to MnO_2 where complete conversion occurs at ca. 750th cycle. The rate of conversion from Mn_3O_4 into MnO_2 is increased 4 times with the addition of GO during potential cycling process. Such rate increment can be attributed to the presence of GO sheets that acted as the electron acceptor which were reduced into rGO upon acceptance of free electron [40,41]. Therefore, the Mn oxidation was not merely based on the electron transfer into the electrode during anodic scan, but it was also enhanced by the electron transfer into electron-acceptor GO sheets. The remaining GO sheets which did not take part in the Mn oxidation were reduced during the cathodic scan [42]. The mechanism

of MnO_2/rGO formation is illustrated in Schematic S1 (Supporting Information).

The conversion of Mn_3O_4 into MnO_2 is confirmed by the XRD analysis (Fig. 2). The detected diffraction peaks show the formation of ramsdellite MnO_2 phase in both MnO_2 and MnO_2/rGO, according to ICCD card (96-900-1168). The additional low-intensity peak at ca. 26° for MnO_2/rGO can be associated with the graphene (002) plane [43]. The low degree of graphitization is due to the surface coverage by MnO_2 species [44]. According to Scherrer equation, the crystallite size of MnO_2 was calculated to be 37 and 19 nm for MnO_2 and MnO_2/rGO, respectively. The smaller crystallite size in MnO_2/rGO can be attributed to the GO sheets which provide a platform for the distribution of Mn_3O_4 particles, prior to potential cycling conversion. Such even distribution can prevent agglomeration and lead to smaller crystallite size formation, as seen in FESEM and TEM analyses (Fig. 3a and b). It can be seen that the MnO_2 particles were evenly distributed on the rGO sheets. The particles size distribution was calculated and presented in Fig. 3c. The mean particles size value was obtained by the Gaussian fitting and found to be 21 nm for MnO_2/rGO, which is very close to those obtained from XRD data. It is noteworthy to highlight that the electron transfer between GO and Mn_3O_4 did not occur in the absence of external electrical potential, as shown in Fig. S1 where Mn_3O_4 in Mn_3O_4/GO mixture remained at its phase in XRD analysis. This is also consistent with other reported works [45,46]. Upon electron transfer occurred between GO and Mn_3O_4, the interaction can be observed from FTIR analysis (Fig. 4a) where additional absorption band can be found at $1110\,cm^{-1}$ for MnO_2/rGO sample, which can be associated to the bending vibration of C–OH combined with Mn atoms [47]. This interaction cannot be seen in MnO_2 sample. In addition, the disappearance of C=O stretching vibration band ($1720\,cm^{-1}$) in MnO_2/rGO also indicates the successful

Table 1
Comparison of reported specific capacitance values to MnO_2/rGO nanocomposite.

Material	Specific capacitance ($F\,g^{-1}$)		Reference
	Cyclic voltammetry	Charge-discharge	
Graphene-ZnO nanocomposites	156 @ $5\,mV\,s^{-1}$	196 @ $0.8\,mA\,cm^{-2}$	[32]
Graphene–TiO_2 nanostructure	165 @ $5\,mV\,s^{-1}$	–	[50]
Graphene-honeycomb MnO_2	170 @ $10\,mV\,s^{-1}$	210 @ $0.5\,A\,g^{-1}$	[36]
Mn_3O_4/graphene nanocomposites	175 @ $5\,mV\,s^{-1}$	–	[43]
Graphene/VOx-NTs	188 @ $50\,mV\,s^{-1}$	210@ $1\,A\,g^{-1}$	[51]
MnO_2 nanorods/graphene	218 @ $5\,mV\,s^{-1}$	–	[52]
Graphene–MnO_2 composites	310 @ $2\,mV\,s^{-1}$	–	[44]
SnO_2/graphene	363.3 @ $10\,mV\,s^{-1}$	364.3 @ $1\,A\,g^{-1}$	[31]
Graphene oxide-MnO_2	–	216 @ $0.15\,A\,g^{-1}$	[30]
Fe_3O_4/graphene nanocomposites	–	220.1 @ $0.5\,A\,g^{-1}$	[29]
Multilayered graphene/ MnO_2	–	252 @ $2\,A\,g^{-1}$	[53]
MnO_2-graphene	–	305 @ $1\,A\,g^{-1}$	[37]
MnO_2-graphene	378 @ $1\,mV\,s^{-1}$	–	[20]
SnO_2 coated MnO_2	–	248.4 @ $0.6\,A\,g^{-1}$	[54]
Sb-doped SnO_2 coated MnO_2	–	292.6 @ $0.6\,A\,g^{-1}$	[54]
Co_3O_4 nanoplate/ graphene	–	337.2 @ $0.2\,A\,g^{-1}$	[33]
Cobalt doped MnO_2	302 @ $10\,mV\,s^{-1}$	415 @ $0.2\,A\,g^{-1}$	[55]
MnO_2/CNFs	329 @ $2\,mV\,s^{-1}$	312 @ $1\,A\,g^{-1}$	[19]
MnO_2/CNTs–CNFs	374 @ $2\,mV\,s^{-1}$	357 @ $1\,A\,g^{-1}$	[19]
MnO_2/C@Si	–	240.1 @ $1\,A\,g^{-1}$	[56]
Co_3O_4-MnO_2	419 @ $5\,mV\,s^{-1}$	–	[21]
MnO_2/rGO	–	*473 @ 0.25 A g^{-1}*	*this work*

electrochemical reduction of GO into rGO as this band is obviously seen in the composite prior to the cycling process (Fig. S2). For further investigation of the structural characteristics of the prepared MnO_2/rGO nanocomposite, Fig. 4b shows Raman spectra of MnO_2 and MnO_2/rGO. The formation of MnO_2 is supported by Mn-O symmetric stretching vibrations of MnO_6 octahedron at ca. $645\,cm^{-1}$ [48]. For MnO_2/rGO, apart from MnO_6 octahedron band, two additional D and G bands appear at ca. 1354 and $1583\,cm^{-1}$, respectively. This indicates the formation of rGO and the intensity ratio I_D/I_G was found to be 0.84, to indicate the disorder degree in rGO structure.
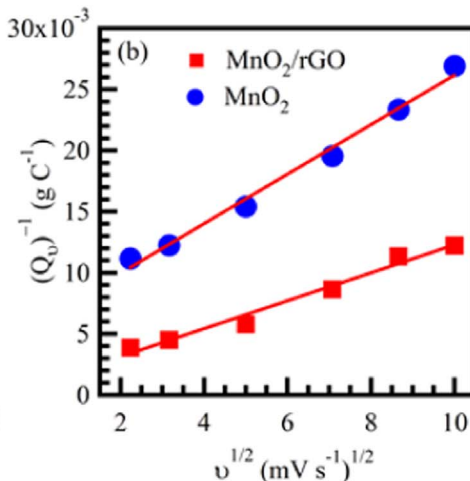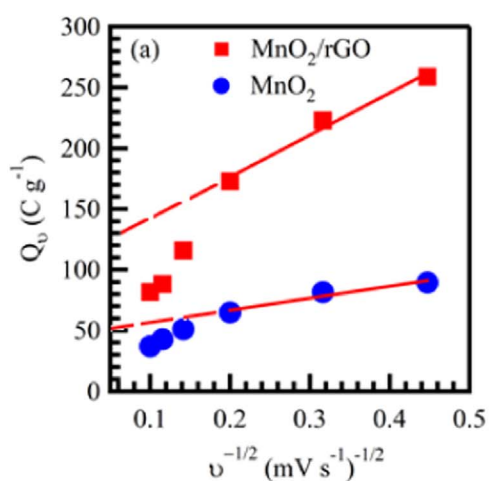
Electrochemical tests were conducted to evaluate the charge storage properties of MnO_2/rGO. The cyclic voltammetry results of MnO_2 and MnO_2/rGO are shown in Fig. 5a. Both samples exhibit rectangular shape in CV curves, indicating the good charge propagation in the electrodes and the absence of redox activity on the electrode surface. The effect of rGO in MnO_2 is significant in electrochemical studies as MnO_2/rGO shows larger area under the CV curve, as compared to that of MnO_2. A CV with larger area under the curve indicates the higher specific capacitance. The samples were further probed with galvanostatic charge-discharge tests in order to simulate the practical operation of the supercapacitors (Fig. 5b and c). Both MnO_2 and MnO_2/rGO electrodes show and symmetrical and linear charge-discharge curves with neglected *iR* drop. The specific capacitance values were calculated as reported elsewhere [12] and the values are summarized against current density in Fig. 5d. For both samples, ions diffusion within the electrode was dominant in the charge storage process as they show current-dependent specific capacitance values where specific capacitance values drop at increasing current density. The highest capacitance of $473\,F\,g^{-1}$ was attained on MnO_2/rGO electrode at $0.25\,A\,g^{-1}$, approximately twice as compared to that of MnO_2 electrode ($257\,F\,g^{-1}$) and around three times as compared to the Mn_3O_4/GO composite prior electrochemical conversion ($180\,F\,g^{-1}$, Fig. S3). The results are compared with other reported works for MnO_2 composites (Table 1) and MnO_2/rGO in this work shows superiority over other reported MnO_2 composites. In addition, the low performance of Mn_3O_4/GO prior conversion signifies the importance of externally applied potential in electron transfer between GO and Mn_3O_4 in MnO_2/rGO synthesis. This is also parallel with XRD findings. Moreover, the bare Ni foam contribution was investigated by testing CV and CDC for Ni foam electrode under the similar experimental conditions. As shown in Fig. S4, bare Ni foam shows very low current with very narrow CV curve (Fig. S4(a)) and very fast discharge time (Fig. S4(b)), giving specific capacitance value less than $0.5\,F\,g^{-1}$. Therefore, the contribution of Ni foam substrate in the electrochemical performance can be neglected as reported before [49].

The kinetics of charge storage in MnO_2 and MnO_2/rGO were studied by Trasatti's analysis. The total stored charge in an electrode can be divided into three fractions: the faradaic contribution from the slow H^+ ions insertion process which is limited by solid-state ion diffusion, the faradaic contribution from the fast charge-transfer process at surfaces or known as pseudocapacitance, and the non-faradaic contribution from the fast electric double layer effect [57]. The former one is regarded as diffusive charge storage while the latter two are known as capacitive charge storage. In Trasatti's analysis, the charge storage processes can be represented by the following equations [58,59]:

$$Q_{(v)} = Q_C + \alpha v^{-1/2} \tag{1}$$

Fig. 6. Dependence of (a) $Q_{(v)}$ on $v^{-1/2}$ and (b) $1/Q_{(v)}$ on $v^{1/2}$ for MnO_2 and MnO_2/rGO.
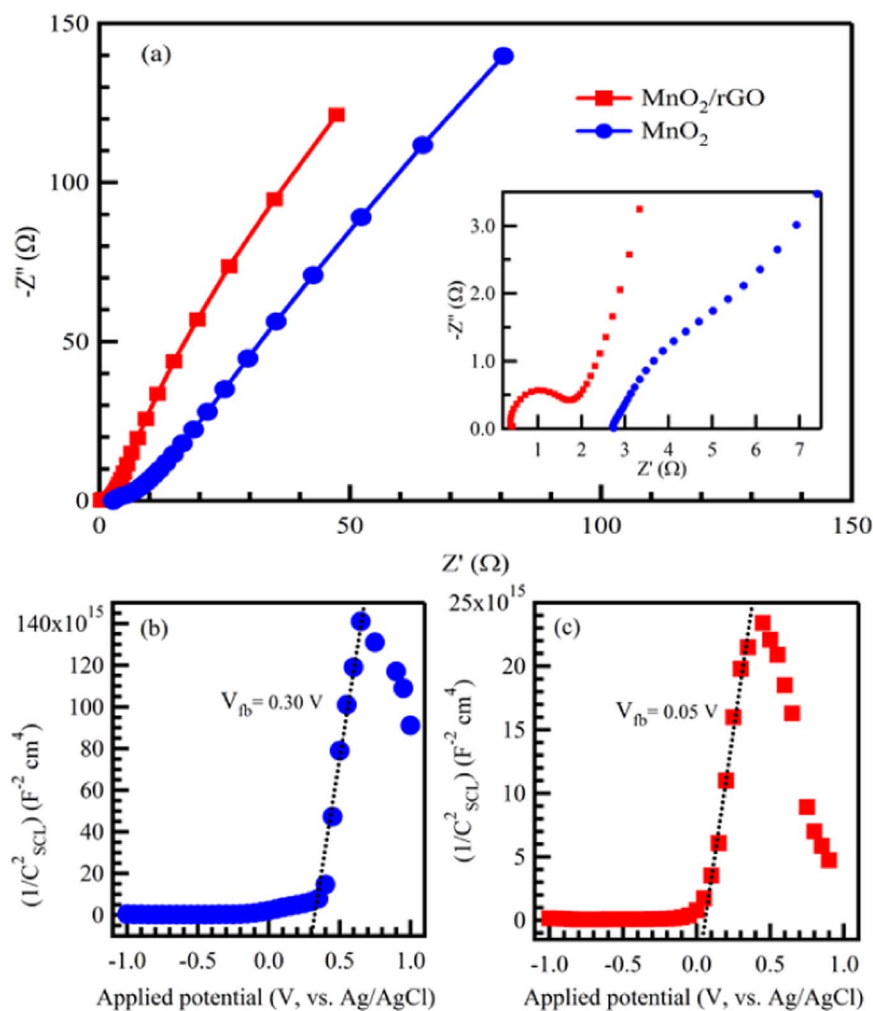
Fig. 7. (a) Nyquist plots for MnO_2 and MnO_2/rGO: the inset is the high–frequency region of the plots and Mott-Schottky plots of (b) MnO_2 and (c) MnO_2/rGO.
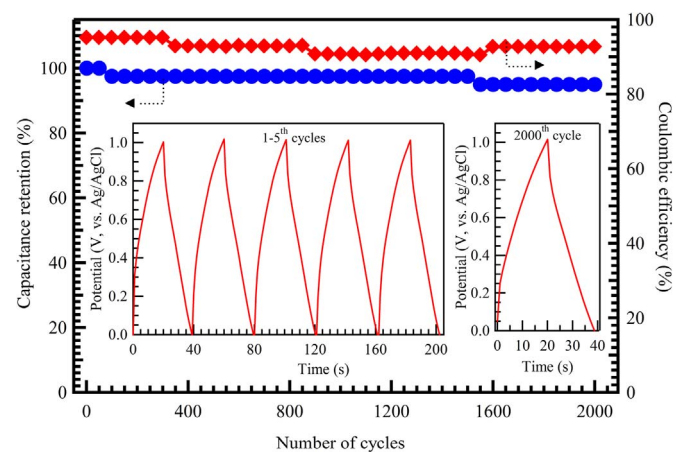
Fig. 8. Cycle life stability curve (left *vs.* bottom) and Coulombic efficiency (right *vs.* bottom) at 3 A g^{-1} current density for MnO_2/rGO, the insets show the charge-discharge curves at different cycle number.

$$1/Q_{(\upsilon)} = 1/Q_T + \alpha \upsilon^{1/2} \tag{2}$$

Where $Q_{(\upsilon)}$ is the total measured voltammetric charge, Q_C is the capacitive charge (from both double layer and pseudocapacitive processes), Q_T is the total amount of stored charge, α is a constant and υ represents the scan rate. In Eq. (1), the diffusive charge storage can be excluded as υ approaches infinite, therefore extrapolating the plot of $Q_{(\upsilon)}$ vs $\upsilon^{-1/2}$ (Fig. 6a) gives the capacitive charge storage (Q_C) at intercept. In Eq. (2),

as the υ approaching 0, the electrochemical reaction time-scale is long enough to allow ions to access to all sites in the electrode and the extrapolation of $1/Q_{(\upsilon)}$ vs $\upsilon^{1/2}$ (Fig. 6b) allows the calculation of Q_T at intercept. The diffusive charge storage (Q_D) can be obtained from the difference between Q_T and Q_C. As shown in Table S1, it can be seen that the contribution of diffusive charge storage in MnO_2 and MnO_2/rGO are 72.4% and 91.4%, respectively. Our previous studies reported that the charge storage of MnO_2 is based on the intercalation/de-intercalation of cations on the structure [9,12,13]. Higher diffusive charge storage in MnO_2/rGO means more cations intercalation/de-intercalation processes that contribute to larger charge storage (higher specific capacitance). It can be attributed to finer MnO_2 particles that were evenly distributed on the rGO sheets and it caused easier ions diffusion process in the structure. The facile diffusion process in MnO_2/rGO can also be identified in Nyquist plot (Fig. 7a) where MnO_2/rGO is having shorter Warburg diffusion which is pertaining to the diffusion resistance of electrolyte within electrode structure. The zoomed view of the high-frequency region in Nyquist plots renders the estimation of equivalent series resistance (ESR) at intercept and charge transfer resistance (R_{CT}) at the semicircle plot. The ESR and R_{CT} are estimated to be 2.84 and 2.33 Ω for MnO_2; and 0.22 and 1.46 Ω for MnO_2/rGO, respectively. The lower ESR and R_{CT} values for MnO_2/rGO can be associated with the presence of rGO in the composite which can improve the conductivity of semiconducting MnO_2. The impedance data was used for the calculation of electroactive surface area, according to the method reported elsewhere [12,13,24,60]. It is noteworthy to highlight that the electroactive surface area for MnO_2/rGO was calculated to be 1173 m^2 g^{-1}, which is approximately 25 times higher than that of MnO_2 (46 m^2 g^{-1}).

Table 2
Comparison of reported cycling stability and Coulombic efficiency with MnO_2/rGO nanocomposite.

Material	Cycling stability (%)	Coulombic efficiency (%)	Reference
MnO_2	88.0 @ 900 cycles	–	[9]
	93.0 @ 1650 cycles	–	[12]
5% Co-MnO_2	97.3 @ 5000 cycles	–	[55]
Bare MnO_2	92.8 @ 5000 cycles	–	
Pure MnO_2 (P-MnO_2)	77.2 @ 1000 cycles	94.2 @ 1000 cycles	[54]
SnO_2-coated MnO_2 (S-MnO_2)	81.1 @ 1000 cycles	95.8 @ 1000 cycles	
Sb-doped SnO_2 (SS-MnO_2)	88.4 @ 1000 cycles	99.0 @ 1000 cycles	
MnO_2/CNTs–CNFs	94.0 @ 1000 cycles	–	[19]
Co_3O_4 nanoplate/graphene sheet	93.2 @ 1000 cycles	–	[33]
Graphene/VOx nanotubes	48.0 @ 5000 cycles	–	[51]
Graphene-ZnO	94.0 @ 5000 cycles	–	[32]
Graphene-TiO_2	91.0 @ 5000 cycles	96.0 @ 5000 cycles	[50]
Graphene nanosheet	86.0 @ 1100 cycles	88.0 @ 1100 cycles	[24]
Graphene-MnO_2	78.0 @ 1000 cycles	–	[38]
Cobalt-MnO_2/carbon-nanofiber	95.0 @ 6000 cycles	–	[21]
Graphene-honeycomb MnO_2	82.4 @ 1000 cycles	–	[36]
Graphene-MnO_2	95.4 @ 15,000 cycles	–	[44]
Graphene oxide-MnO_2	84.1 @ 1000 cycles	–	[30]
Bare MnO_2	69.0 @ 1000 cycles	–	
MnO_2 on nickel foam-graphene	–	80.0 @ 1000 cycles	[37]
Graphene/MnO_2	96.0 @ 6000 cycles	–	[53]
Bare MnO_2	96.0 @ 6000 cycles	–	
RGO-wrapped MnO_2	83.0 @ 1000 cycles	–	[20]
MnO_2 nanorods/graphene	93.8 @ 1000 cycles	94.0 @ 1000 cycles	[52]
MnO_2/rGO	***95 @ 2000 cycles***	***92 @ 2000 cycles***	*this work*

It can be deduced that rGO sheets provided a huge platform for the distribution of MnO_2 and therefore prevented their agglomeration, as seen from TEM analysis too. It also supports the electrochemical findings to suggest the diffusive charge storage to be the dominant charge storage mechanism in MnO_2/rGO where more diffusion process occurred in MnO_2/rGO with high electroactive surface area. The electrical conductivity was further investigated by performing potential-dependent capacitance measurements at a frequency of 450 Hz. The capacitance C is then calculated from the imaginary part of the impedance: C = $-1/\omega Z''$ where $\omega = 2\pi f$, and Z'' represents the imaginary impedance. According to Mott-Schottky theory, the capacitance of the space charge layer is expressed as [12,61,62]:

$$\frac{1}{C_{SCL}^2} = \frac{2}{e\varepsilon\varepsilon_o N_D}\left(V - V_{fb} - \frac{kT}{e}\right) \tag{3}$$

where C_{SCL} is the capacitance of the space charge layer, e is the charge of electron, ε_o is free space permittivity (8.85×10^{-14} F cm^{-1}), ε is dielectric constant (32 for MnO_2 [63]), V is applied potential, V_{fb} is flat-band potential, N_D is donor density or donor concentration, k is Boltzmann constant, T is Kelvin temperature. As seen from Fig. 7b and c, both MnO_2 and MnO_2/rGO exhibit a strong capacity dependence towards applied voltage, which indicates the space charge layer controlled capacity of a semiconductor in the electrolyte. The flat-band potential of MnO_2 and MnO_2/rGO were calculated to be 0.30 and 0.05 V, respectively. The negative shift of the V_{fb} in MnO_2/rGO indicates a shift of conduction band to more positive potentials, which lead to enhanced electrical conductivity of the electrodes. To understand the impact of rGO in MnO_2 in terms of electrical conductivity quantitatively, carrier density for both MnO_2 and MnO_2/rGO was calculated. As expected, the semiconducting MnO_2 possesses carrier density of 7.6×10^{12} cm^{-3} and MnO_2/rGO shows significant increased carrier density of 74.4×10^{12} cm^{-3}. The enhancement in carrier density can be attributed to the electron donation of electron-rich rGO to MnO_2 [61].

The long-term potential cycling stability is a very important factor in supercapacitor applications. As shown in Fig. 8 (left *vs.* bottom), MnO_2/rGO shows high cycling stability, reaching 95% of its original values at 3 A g^{-1} after 2000 cycles. After 1500 cycle, only 2.5% capacitance loss is shown and it is less than the capacitance loss of other reported MnO_2 graphene composites such as hydrothermally prepared

MnO_2 nanorods/graphene [52], graphene-wrapped honeycomb MnO_2 nanospheres [36] and RGO-wrapped MnO_2 composite [20]. The inset of Fig. 8 shows the representative charge-discharge curves remain linear throughout the stability test cycles, indicating an insignificant change in the specific capacitance of MnO_2/rGO and renders its long-term stability. In addition, MnO_2/rGO shows a high Coulombic efficiency of 92% after 2000 cycles, which is higher than those reported elsewhere [24,64]. The cycling stability and Coulombic efficiency of the prepared MnO_2/rGO nanocomposite were compared with the reported values of similar materials as listed in Table 2.

4. Conclusions

The current work reports on the one-step electrosynthesis of MnO_2/rGO from Mn_3O_4 and GO mixture. The electro-oxidation of Mn_3O_4 into MnO_2 is expedited by the electron transfer process into the electron-accepting GO sheets and therefore reducing GO into rGO. The MnO_2/rGO shows high specific capacitance of 473 F g^{-1} at 0.25 A g^{-1}, which is predominantly associated with the presence of rGO. In MnO_2/rGO, rGO sheets act as the platform for even distribution of MnO_2 nanoparticles; MnO_2 acts as the spacer to prevent rGO sheets from stacking. Such unique structure provides high electroactive surface area (1173 m^2 g^{-1}) in which improves the ions diffusion within MnO_2/rGO structure and contributes to huge diffusive charge storage. The presence of rGO also improves the conductivity of semiconducting MnO_2 and increases the carrier density, as shown in electrochemical impedance spectroscopy. The electro-generated MnO_2/rGO also presents high cycling stability up to 2000 cycles. These findings suggest the one-step electrochemical approach can produce MnO_2/rGO that can be the potential electrode material for highly stable supercapacitors.

Appendix A. Supporting information

Supplementary data associated with this article can be found in the online version at http://dx.doi.org/10.1016/j.ceramint.2018.01.212.

References

[1] P. Simon, Y. Gogotsi, Materials for electrochemical capacitors, Nat. Mater. 7 (2008) 845–854.

[2] G.A.M. Ali, S.A.B.A. Manaf, A. Kumar, K.F. Chong, G. Hegde, High performance supercapacitor using catalysis free porous carbon nanoparticles, J. Phys. D: Appl. Phys. 47 (2014) 495307–495313.

[3] G.A.M. Ali, O.A. Fouad, S.A. Makhlouf, M.M. Yusoff, K.F. Chong, Co_3O_4/SiO_2 nanocomposites for supercapacitor application, J. Solid State Electrochem. 18 (2014) 2505–2512.

[4] G.A.M. Ali, E.Y. Lih Teo, E.A.A. Aboelazm, H. Sadegh, A.O.H. Memar, R. Shahryari-Ghoshekandi, K.F. Chong, Capacitive performance of cysteamine functionalized carbon nanotubes, Mater. Chem. Phys. 197 (2017) 100–104.

[5] J. Wu, X. Gao, H. Yu, T. Ding, Y. Yan, B. Yao, X. Yao, D. Chen, M. Liu, L. Huang, A scalable free-standing V_2O_5/CNT film electrode for supercapacitors with a wide operation voltage (1.6 V) in an aqueous electrolyte, Adv. Funct. Mater. 26 (2016) 6114–6120.

[6] J. Li, K. Liu, X. Gao, B. Yao, K. Huo, Y. Cheng, X. Cheng, D. Chen, B. Wang, W. Sun, Oxygen-and nitrogen-enriched 3D porous carbon for supercapacitors of high volumetric capacity, ACS Appl. Mater. Interfaces 7 (2015) 24622–24628.

[7] B.E. Conway, Electrochemical Supercapacitors: Scientific Fundamentals And Technological Applications, Springer Science & Business Media, 2013.

[8] G.A.M. Ali, D. Aravind, S. Supriya, K.F. Chong, A. Ethiraj, M. Reddy, H. Gharni, G. Hegde, Carbon nanospheres derived from Lablab Purpureus as a high performance supercapacitor electrode: Green approach, Dalton Trans. 46 (2017) 14034–14044.

[9] G.A.M. Ali, L.L. Tan, R. Jose, M.M. Yusoff, K.F. Chong, Electrochemical performance studies of MnO_2 nanoflowers recovered from spent battery, Mater. Res. Bull. 60 (2014) 5–9.

[10] B. Ming, J. Li, F. Kang, G. Pang, Y. Zhang, L. Chen, J. Xu, X. Wang, Microwave–hydrothermal synthesis of birnessite-type MnO_2 nanospheres as supercapacitor electrode materials, J. Power Sources 198 (2012) 428–431.

[11] S.C. Pang, M.A. Anderson, T.W. Chapman, Novel electrode materials for thin-film ultracapacitors: comparison of electrochemical properties of sol-gel-derived and electrodeposited manganese dioxide, J. Electrochem. Soc. 147 (2000) 444–450.

[12] G.A.M. Ali, M.M. Yusoff, E.R. Shaaban, K.F. Chong, High performance MnO_2 nanoflower supercapacitor electrode by electrochemical recycling of spent batteries, Ceram. Int. 43 (2017) 8440–8448.

[13] G.A.M. Ali, M.M. Yusoff, Y.H. Ng, H.N. Lim, K.F. Chong, Potentiostatic and galvanostatic electrodeposition of manganese oxide for supercapacitor application: A comparison study, Curr. Appl. Phys. 15 (2015) 1143–1147.

[14] K.V. Sankar, D. Kalpana, R.K. Selvan, Electrochemical properties of microwave-assisted reflux-synthesized Mn_3O_4 nanoparticles in different electrolytes for supercapacitor applications, J. Appl. Electrochem. 42 (2012) 463–470.

[15] C. Ulutas, O. Erken, M. Gunes, C. Gumus, Effect of annealing temperature on the physical properties of Mn_3O_4 thin film prepared by chemical bath deposition, Int. J. Electrochem. Sci. 11 (2016) 2835–2845.

[16] V.C. Bose, V. Biju, Defect dependent optical, electrical and magnetic properties of nanostructured Mn_3O_4, Superlattices Microstruct. 88 (2015) 287–298.

[17] T. Li, J. Wu, X. Xiao, B. Zhang, Z. Hu, J. Zhou, P. Yang, X. Chen, B. Wang, L. Huang, Band gap engineering of MnO_2 through in situ Al-doping for applicable pseudocapacitors, RSC Adv. 6 (2016) 13914–13921.

[18] C. Xu, F. Kang, B. Li, H. Du, Recent progress on manganese dioxide based supercapacitors, J. Mater. Res. 25 (2010) 1421–1432.

[19] J.-G. Wang, Y. Yang, Z.-H. Huang, F. Kang, Synthesis and electrochemical performance of MnO_2/CNTs–embedded carbon nanofibers nanocomposites for supercapacitors, Electrochim. Acta 75 (2012) 213–219.

[20] P.Y. Chan, Rusi, S.R. Majid, RGO-wrapped MnO_2 composite electrode for supercapacitor application, Solid State Ionics 262 (2014) 226–229.

[21] S.H. Kim, Y.I. Kim, J.H. Park, J.M. Ko, Cobalt-manganese oxide/carbon-nanofiber composite electrodes for supercapacitors, Int. J. Electrochem. Sci. 4 (2009) 1489–1496.

[22] M.D. Stoller, S. Park, Y. Zhu, J. An, R.S. Ruoff, Graphene-based ultracapacitors, Nano Lett. 8 (2008) 3498–3502.

[23] Y. Sun, Q. Wu, G. Shi, Graphene based new energy materials, Energy Environ. Sci. 4 (2011) 1113–1132.

[24] G.A.M. Ali, S.A. Makhlouf, M.M. Yusoff, K.F. Chong, Structural and electrochemical characteristics of graphene nanosheets as supercapacitor electrodes, Rev. Adv. Mater. Sci. 41 (2015) 35–43.

[25] G.A.M. Ali, M.M. Yusoff, K.F. Chong, Graphene electrochemical production and its energy storage properties, ARPN J. Eng. Appl. Sci. 11 (2016) 9712–9717.

[26] C. Liu, Z. Yu, D. Neff, A. Zhamu, B.Z. Jang, Graphene-based supercapacitor with an ultrahigh energy density, Nano Lett. 10 (2010) 4863–4868.

[27] X. Wang, G. Shi, Flexible graphene devices related to energy conversion and storage, Energy Environ. Sci. 8 (2015) 790–823.

[28] J. Yang, S. Gunasekaran, Electrochemically reduced graphene oxide sheets for use in high performance supercapacitors, Carbon 51 (2013) 36–44.

[29] Q. Wang, L. Jiao, H. Du, Y. Wang, H. Yuan, Fe_3O_4 nanoparticles grown on graphene as advanced electrode materials for supercapacitors, J. Power Sources 245 (2014)

[30] S. Chen, J. Zhu, X. Wu, Q. Han, X. Wang, Graphene oxide-MnO_2 nanocomposites for supercapacitors, ACS Nano 4 (2010) 2822–2830.

[31] S.P. Lim, N.M. Huang, H.N. Lim, Solvothermal synthesis of SnO_2/graphene nanocomposites for supercapacitor application, Ceram. Int. 39 (2013) 6647–6655.

[32] Z. Li, Z. Zhou, G. Yun, K. Shi, X. Lv, B. Yang, High-performance solid-state supercapacitors based on graphene-ZnO hybrid nanocomposites, Nanoscale Res. Lett. 8 (2013) 1–9.

[33] L. Wang, D. Wang, J. Zhu, X. Liang, Preparation of Co_3O_4 nanoplate/graphene sheet composites and their synergistic electrochemical performance, Ionics 19 (2013) 215–220.

[34] Q. Ke, J. Wang, Graphene-based materials for supercapacitor electrodes – A review, J. Materiomics 2 (2016) 37–54.

[35] P.E. Marina, G.A.M. Ali, L.M. See, E.Y.L. Teo, E.-P. Ng, K.F. Chong, In situ growth of redox-active iron-centered nanoparticles on graphene sheets for specific capacitance enhancement, Arab. J. Chem. (2016), http://dx.doi.org/10.1016/j.arabjc.2016.1002.1006.

[36] J. Zhu, J. He, Facile synthesis of graphene-wrapped honeycomb MnO_2 nanospheres and their application in supercapacitors, ACS Appl. Mater. Interfaces 4 (2012) 1770–1776.

[37] A. Bello, O.O. Fashedemi, M. Fabiane, J.N. Lekitima, K.I. Ozoemena, N. Manyala, Microwave assisted synthesis of MnO_2 on nickel foam-graphene for electrochemical capacitor, Electrochim. Acta 114 (2013) 48–53.

[38] E.R. Ezeigwe, M.T.T. Tan, P.S. Khiew, C.W. Siong, Solvothermal synthesis of graphene–MnO_2 nanocomposites and their electrochemical behavior, Ceram. Int. 41 (2015) 11418–11427.

[39] X. Zhang, P. Yu, D. Zhang, H. Zhang, X. Sun, Y. Ma, Room temperature synthesis of Mn_3O_4 nanoparticles: characterization, electrochemical properties and hydrothermal transformation to γ-MnO_2 nanorods, Mater. Lett. 92 (2013) 401–404.

[40] H.D. Pham, V.H. Pham, E.-S. Oh, J.S. Chung, S. Kim, Synthesis of polypyrrole-reduced graphene oxide composites by in-situ photopolymerization and its application as a supercapacitor electrode, Korean J. Chem. Eng. 29 (2012) 125–129.

[41] I.V. Lightcap, P.V. Kamat, Fortification of CdSe quantum dots with graphene oxide. Excited state interactions and light energy conversion, J. Am. Chem. Soc. 134 (2012) 7109–7116.

[42] L. Chen, Y. Tang, K. Wang, C. Liu, S. Luo, Direct electrodeposition of reduced graphene oxide on glassy carbon electrode and its electrochemical application, Electrochem. Commun. 13 (2011) 133–137.

[43] B. Wang, J. Park, C. Wang, H. Ahn, G. Wang, Mn_3O_4 nanoparticles embedded into graphene nanosheets: Preparation, characterization, and electrochemical properties for supercapacitors, Electrochim. Acta 55 (2010) 6812–6817.

[44] J. Yan, Z. Fan, T. Wei, W. Qian, M. Zhang, F. Wei, Fast and reversible surface redox reaction of graphene–MnO_2 composites as supercapacitor electrodes, Carbon 48 (2010) 3825–3833.

[45] L. Wang, Y. Li, Z. Han, L. Chen, B. Qian, X. Jiang, J. Pinto, G. Yang, Composite structure and properties of Mn_3O_4/graphene oxide and Mn_3O_4/graphene, J. Phys. Chem. A 1 (2013) 8385–8397.

[46] G.S. Gund, D.P. Dubal, B.H. Patil, S.S. Shinde, C.D. Lokhande, Enhanced activity of chemically synthesized hybrid graphene oxide/Mn_3O_4 composite for high performance supercapacitors, Electrochim. Acta 92 (2013) 205–215.

[47] S.G. Hwang, J.E. Hong, G.O. Kim, H.M. Jeong, K.S. Ryu, Graphene anchored with NiO-MnO_2 nanocomposites for use as an electrode material in supercapacitors, ECS Solid State Lett. 2 (2012) M8–M11.

[48] S.-W. Lee, S.-M. Bak, C.-W. Lee, C. Jaye, D.A. Fischer, B.-K. Kim, X.-Q. Yang, K.-W. Nam, K.-B. Kim, Structural changes in reduced graphene oxide upon MnO_2 deposition by the redox reaction between carbon and permanganate ions, J. Phys. Chem. C 118 (2014) 2834–2843.

[49] G.A.M. Ali, O.A.G. Wahba, A.M. Hassan, O.A. Fouad, K.F. Chong, Calcium-based nanosized mixed metal oxides for supercapacitor application, Ceram. Int. 41 (2015) 8230–8234.

[50] A. Ramadoss, S.J. Kim, Improved activity of a graphene–TiO_2 hybrid electrode in an electrochemical supercapacitor, Carbon 63 (2013) 434–445.

[51] M. Fu, C. Ge, Z. Hou, J. Cao, B. He, F. Zeng, Y. Kuang, Graphene/vanadium oxide nanotubes composite as electrode material for electrochemical capacitors, Physica B 421 (2013) 77–82.

[52] S. Deng, D. Sun, C. Wu, H. Wang, J. Liu, Y. Sun, H. Yan, Synthesis and electrochemical properties of MnO_2 nanorods/graphene composites for supercapacitor applications, Electrochim. Acta 111 (2013) 707–712.

[53] M.-S. Wu, C.-J. Lin, C.-L. Ho, Multilayered architecture of graphene nanosheets and MnO_2 nanowires as an electrode material for high-performance supercapacitors, Electrochim. Acta 81 (2012) 44–48.

[54] Y. Zhang, Y. Mo, Preparation of MnO_2 electrodes coated by Sb-doped SnO_2 and their effect on electrochemical performance for supercapacitor, Electrochim. Acta 142 (2014) 76–83.

[55] B.C. Kim, C. Justin Raj, W.-J. Cho, W.-G. Lee, H.T. Jeong, K.H. Yu, Enhanced electrochemical properties of cobalt doped manganese dioxide nanowires, J. Alloy. Compd. 617 (2014) 491–497.

[56] I. Oh, M. Kim, J. Kim, Carbon-coated Si/MnO_2 nanoneedle composites with optimum carbon layer activation for supercapacitor applications, Chem. Eng. J. 273 (2015) 82–91.

[57] T. Brezesinski, J. Wang, S.H. Tolbert, B. Dunn, Ordered mesoporous α-MoO_3 with iso-oriented nanocrystalline walls for thin-film pseudocapacitors, Nat. Mater. 9 (2010) 146–151.

[58] S. Ardizzone, G. Fregonara, S. Trasatti, "Inner" and "outer" active surface of RuO_2 electrodes, Electrochim. Acta 35 (1990) 263–267.

[59] D. Baronetto, N. Krstajić, S. Trasatti, Reply to "note on a method to interrelate inner

and outer electrode areas" by H. Vogt, Electrochim. Acta 39 (1994) 2359–2362.

[60] S. Chou, F. Cheng, J. Chen, Electrodeposition synthesis and electrochemical properties of nanostructured γ-MnO_2 films, J. Power Sources 162 (2006) 727–734.

[61] W.J. Basirun, M. Sookhakian, S. Baradaran, Z. Endut, M.R. Mahmoudian, M. Ebadi, R. Yousefi, H. Ghadimi, S. Ahmed, Graphene oxide electrocatalyst on MnO_2 air cathode as an efficient electron pump for enhanced oxygen reduction in alkaline solution, Sci. Rep. 5 (2015).

[62] T. Giannakopoulou, I. Papailias, N. Todorova, N. Boukos, Y. Liu, J. Yu, C. Trapalis, Tailoring the energy band gap and edges' potentials of g-C_3N_4/TiO_2 composite photocatalysts for NOx removal, Chem. Eng. J. 310 (2017) 571–580.

[63] J.W. Murray, The interaction of metal ions at the manganese dioxide-solution interface, Geochim. Cosmochim. Acta 39 (1975) 505–519.

[64] Z. Lei, J. Zhang, X. Zhao, Ultrathin MnO_2 nanofibers grown on graphitic carbon spheres as high-performance asymmetric supercapacitor electrodes, J. Mater. Chem. 22 (2012) 153–160.